

A PRESSURE-BASED ALGORITHM FOR HIGH-SPEED TURBOMACHINERY FLOWS

E. S. POLITIS AND K. C. GIANNAKOGLOU*

Laboratory of Thermal Turbomachines, National Technical University of Athens, PO Box 64069, Athens 15710, Greece

SUMMARY

The steady state Navier–Stokes equations are solved in transonic flows using an elliptic formulation. A segregated solution algorithm is established in which the pressure correction equation is utilized to enforce the divergence-free mass flux constraint. The momentum equations are solved in terms of the primitive variables, while the pressure correction field is used to update both the convecting mass flux components and the pressure itself. The velocity components are deduced from the corrected mass fluxes on the basis of an upwind-biased density, which is a mechanism capable of overcoming the ellipticity of the system of equations, in the transonic flow regime. An incomplete LU decomposition is used for the solution of the transport-type equations and a globally minimized residual method resolves the pressure correction equation. Turbulence is resolved through the k – ϵ model. Dealing with turbomachinery applications, results are presented in two-dimensional compressor and turbine cascades under design and off-design conditions. © 1997 by John Wiley & Sons, Ltd.

Int. J. Numer. Meth. Fluids, **25**: 63–80 (1997).

No. of Figures: 11. No. of Tables: 1. No. of References: 17.

KEY WORDS: turbulent flows; compressible flows; pressure correction; approximate factorization; density biasing

INTRODUCTION

When elliptic solvers are extended to cover compressible flow problems including supersonic zones, mechanisms overcoming the ellipticity of the scheme needs to be introduced locally. In pressure-based methods which are of interest herein, all these special treatments must be viewed in relation to the static pressure itself and its role in flows with Mach number exceeding the ‘incompressible’ flow limit. In these flow regions, in fact, the pressure undertakes a dual role. It still retains the responsibility for numerically coupling the pressure and velocity fields, which is a key element in incompressible flows. In addition, the pressure couples with the density through the state equation.

Special treatments can be generally envisaged in the form of selective modifications to the standard central difference scheme used for the discretization of the pressure and velocity (or mass flux) spatial differences in the momentum and continuity equations respectively. Needless to say, the convection terms, being always treated through upwind schemes of different levels of accuracy, are the only terms which are properly treated regardless of the level of Mach number. Aiming at an exact modelling of the physical way information is propagating, upstream differences seem to be theoretically needed for all the aforementioned terms. Upwind biasing may apply on different quantities involved in the calculation procedure (the pressure and/or the density, for instance) and in

* Correspondence to: K. C. Giannakoglou, Laboratory of Thermal Turbomachines, National Technical University of Athens, PO Box 64069, Athens 15710, Greece.

different ways for collocated or staggered grids. Depending on how upwinding is introduced, more or less smeared discontinuities may appear.

Some important contributions to this problem are listed below. On a staggered grid, Issa and Lockwood¹ extended a pressure-based elliptic solver to high-speed flows by upwinding both the pressure gradient and the density; the erroneous ellipticity was removed, but uncontrolled artificial dissipation was introduced. Karki and Patankar² solved the momentum equations in the velocity components by handling the continuity equation as a first-order upwinded transport equation for the density. McGuirk and Page³ solved the unsteady form of the equations in the mass flux components on a staggered grid; shock capturing was achieved by solving the pressure correction equation for the retarded pressure. Zhou and Davidson⁴ solved the steady flow equations in the primitive velocity components on a collocated grid by first-order upwinding the density and density corrections appearing in the pressure correction equation. The calculated 1D transonic solutions were very dissipative owing to the low-order upwind of density and density corrections. Demirdzic *et al.*⁵ used the SIMPLE algorithm on a collocated grid to solve the momentum equations in terms of the velocity components, while the mass flux at the cell faces was upwind biased, though partially blended with a central scheme.

On a collocated grid, Lien and Leschziner⁶ used the time-dependent flow equations and density-weighted variables, which are expected to undergo smoother variations than the primitive variables themselves. A third-order pressure-smoothing term is added in the convecting mass flux components at the midfaces. Extra numerical dissipation is added through the retarded density. The latter is indirectly introduced in the contravariant velocity components, which are in turn involved in all transport equations.

Compared with the aforementioned works, the present method makes use of a collocated grid system where all primitive variables are stored in cell-centred storage. In fact, the present method is an extension of the segregated solution algorithm, previously used for the numerical solution of the steady incompressible Navier–Stokes equations,⁷ to the transonic regime. As in the incompressible flow solver, the momentum equations are still solved in terms of the Cartesian velocity components. The pressure correction is linked to the mass fluxes which comprise the convecting field; as such, the mass fluxes are distinguished from the velocity components and stored at the midfaces of the control volumes. The velocity variables at the cell centres are in turn corrected by combining the pressure correction field with an upwind-biased density, intentionally violating the ellipticity of the equations in supersonic regions. For the implementation of the k - ε turbulence model, transport-type equations are solved using the same coefficient matrix as for the momentum equations, with no additional inversion cost. The numerical solution of all discretized equations is carried out by means of fast implicit solvers, appropriately modified to account for the periodicity conditions. The capabilities of the proposed method are demonstrated in the analysis of a compressor and a turbine cascade under various flow conditions.

GOVERNING EQUATIONS

Under certain assumptions the steady fluid flow can be analyzed without considering the energy equation and consequently the mass and momentum conservation laws alone specify the problem. In a Cartesian co-ordinate system (x_i , $i = 1, 2$) these are written in the form⁸

$$\frac{\partial}{\partial x_j} (h\rho u_j) = 0, \quad (1)$$

$$\frac{\partial}{\partial x_j} (h\rho u_i u_j) = -\frac{\partial}{\partial x_i} [h(p + \frac{2}{3}\rho k)] + \frac{\partial}{\partial x_j} \left[h(\mu + \mu_t) \left(\frac{\partial u_i}{\partial x_j} + \frac{\partial u_j}{\partial x_i} \right) - \frac{2}{3} h(\mu + \mu_t) \delta^{ij} \frac{\partial u_k}{\partial x_k} \right] + S_h^i, \quad i = 1, 2, \quad (2)$$

where u_i ($i = 1, 2$) are the Cartesian velocity components, ρ is the fluid density, μ is the molecular viscosity and p is the static pressure. Throughout this work a repeated index denotes summation over all spatial components. The streamtube thickness h is included in (1) and (2) to account for its varying distribution appearing in one of the examined cases. Owing to the thickness variation in the x_1 -direction, additional source terms S_h^i appear, namely

$$S_h^1 = \frac{dh}{dx_1} \left(p - 2(\mu + \mu_t) \frac{u_1}{h} \frac{dh}{dx_1} - \frac{2}{3}(\mu + \mu_t) \frac{\partial u_k}{\partial x_k} \right), \quad S_h^2 = 0.$$

Since the scope of this work is rooted principally in turbulent flow modelling, the eddy viscosity μ_t and the turbulent kinetic energy k have already been introduced in (2). According to the high-Reynolds-number k - ε turbulence model, μ_t is related to k and to the energy dissipation ε through the expression

$$\mu_t = c_\mu \rho \frac{k^2}{\varepsilon}, \quad c_\mu = 0.09. \quad (3)$$

For k and ε , typical transport equations with non-zero source terms are introduced in the form

$$\frac{\partial}{\partial x_j} (h \rho u_j \Phi) = \frac{\partial}{\partial x_j} \left(h \frac{\mu_t}{\sigma_\Phi} \frac{\partial \Phi}{\partial x_j} \right) + S^\Phi, \quad \Phi = k, \varepsilon, \quad (4)$$

where

$$S^k = (G - \rho \varepsilon) h, \quad S^\varepsilon = (c_1 G - c_2 \rho \varepsilon) \frac{\varepsilon}{k} h.$$

Following the Jones and Launder model,⁹ the constants appearing in the ε equation's source term are $c_1 = 1.43$ and $c_2 = 1.92$, while the effective Prandtl numbers have the values $\sigma_k = 1.0$ and $\sigma_\varepsilon = 1.3$. The production rate of turbulence G is modelled through the formula

$$G = \mu_t \left(\frac{\partial u_i}{\partial x_k} + \frac{\partial u_k}{\partial x_i} \right) \frac{\partial u_i}{\partial x_k} - \frac{2}{3} \frac{\partial u_j}{\partial x_j} \left(\mu_t \frac{\partial u_\lambda}{\partial x_\lambda} + \rho k \right).$$

When compressibility effects are encountered, the equation of state for an ideal gas is used to couple the thermodynamic properties in the form

$$p = R \rho T, \quad (5)$$

where T is the static temperature and R is the gas constant ($R = 287.04 \text{ m}^2 \text{ s}^{-2} \text{ K}^{-1}$). The total temperature is assumed to remain constant over the whole field and is related to the kinematic quantities through the expression

$$T_t = T + \frac{1}{2C_p} (u_i u_i + 2k), \quad (6)$$

where C_p is the specific heat at constant pressure.

GEOMETRICAL TRANSFORMATION

In order to handle complex geometries, a body-fitted curvilinear co-ordinate system ξ^i , $i = 1, 2$, is introduced and all governing equations are transformed accordingly. If J and \vec{g}^j are the Jacobian of the transformation and the contravariant base vectors respectively,

$$J = \frac{\partial(x_1, x_2)}{\partial(\xi^1, \xi^2)}, \quad \vec{g}^j = \nabla \xi^j,$$

the governing equations are cast in the form

$$\frac{\partial}{\partial \xi^j} (h \rho J V^j) = 0, \quad (7)$$

$$\frac{\partial}{\partial \xi^j} (h \rho J V^j u_i) = \frac{\partial}{\partial \xi^j} \left(h (\mu + \mu_t) J g^{jk} \frac{\partial u_i}{\partial \xi^k} \right) - J \frac{\partial}{\partial x_i} \left[h \left(p + \frac{2}{3} \rho k \right) \right] - \frac{2}{3} J \frac{\partial}{\partial x_j} \left(h (\mu + \mu_t) \delta^{ij} \frac{\partial u_k}{\partial u_k} \right) + S_h^i, \quad (8)$$

$i = 1, 2,$

$$\frac{\partial}{\partial \xi^j} (h \rho J V^j \Phi) = \frac{\partial}{\partial \xi^j} \left(h \frac{\mu_t}{\sigma_\Phi} J g^{jk} \frac{\partial \Phi}{\partial \xi^k} \right) + S^\Phi, \quad \Phi = k, \varepsilon, \quad (9)$$

where $g^{jk} = \vec{g}^j \cdot \vec{g}^k$ stands for the contravariant metric tensor, V^j are the contravariant velocity components. The latter are defined as the inner product of the velocity vector and the contravariant base vector, namely

$$V^j = \vec{V} \cdot \vec{g}^j, \quad i = 1, 2.$$

BOUNDARY CONDITIONS

In order to obtain a well-posed problem, the boundary conditions must comply with the physics of the flow. For compressible fluid flows with subsonic inlet the mass flow rate is indirectly defined by means of the inlet flow angle along with the inlet total and the exit static pressure. The total temperature is also imposed and kept constant in the whole field, which, among other things, assumes that the solid boundaries are considered adiabatic. The static pressure at the inlet is extrapolated from the interior of the field. At the exit plane where the static pressure is imposed, the velocity obeys a zero-gradient law and so do k and ε . At the inlet the turbulence quantities are prescribed by means of the turbulence intensity and a mixing length.

Since the high-Reynolds-number $k-\varepsilon$ model is coupled with the wall function technique, the turbulent log-law applies to velocity components at nodes adjacent to solid boundaries. The wall function technique also provides exact relations for k and ε at the same nodes. The static pressure is calculated through a zero-gradient boundary condition. Along periodic boundaries, periodicity is imposed.

DISCRETIZATION OF EQUATIONS

According to the cell-centred discretization scheme adopted, the governing equations are integrated by applying the Gauss theorem over control volumes enclosed by adjacent grid lines. All solution variables are stored over the centres of the cells and, apart from the Cartesian velocity components, linear interpolation is used for the calculation of any other flow variable over the cell faces. For the Cartesian velocity components a pressure-weighted interpolation scheme¹⁰ is incorporated which is capable of alleviating any pressure-velocity decoupling. On the other hand, in supersonic regions the

density is upwinded in order to account for the modified type of governing equations, but its discussion is deferred to a later paragraph.

Momentum equations

According to the notation provided in Figure 1, the momentum equations integrated over an arbitrary control volume yield

$$\left[Jh(\mu + \mu_t)g^{11} \frac{\partial u_i}{\partial \xi^1} - Jh\rho V^1 u_i - Jh \frac{\partial \xi^1}{\partial x_i} p \right]_w^e + \left[Jh(\mu + \mu_t)g^{22} \frac{\partial u_i}{\partial \xi^2} - Jh\rho V^2 u_i - Jh \frac{\partial \xi^2}{\partial x_i} p \right]_b^f = C^i, \quad i = 1, 2, \quad (10)$$

where C^i consist of both the cross-diffusion terms which include the g^{ij} ($i \neq j$) metrics and the extra source terms in (8). The cross-diffusion terms are treated explicitly, as the convergence acceleration resulting from their implicit treatment does not compensate for the extra computing cost. Equations (10) can be recast in various alternative forms depending on the selection of the solution variables. In the literature, formulations based on both the Cartesian velocity components and the mass fluxes ρu_i appear.⁴⁻⁶ From a theoretical point of view the use of the density-velocity product seems advantageous since it undergoes smoother variations, but this is generally outperformed by the additional mechanism needed to separate velocities from density. In the present work the momentum equations are solved in terms of the Cartesian velocity components by assuming the most recent p and ρ fields. This approach must be distinguished from the aforementioned ones (e.g. Reference 6) since here the convecting field is expressed by the ρV^j products. These are finally required at the cell faces and are the outcome of the pressure correction step at the end of the preceding iteration. As will be shown in equation (14), the convecting field depends only indirectly upon the upwind-biased density. In contrast with Reference 3, pressure gradients are centrally differenced and thus the use of dissipative pressure-retarded schemes is avoided.

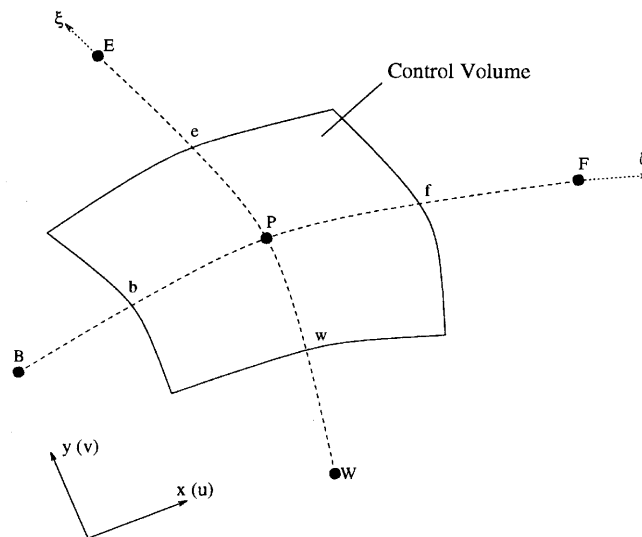


Figure 1. Two-dimensional control volume and corresponding notation

An implicit discretization of the left-hand side of (10) gives rise to a five-node stencil. The coefficients involved are the same for all momentum equations and depend on the convecting mass fluxes, the metrics of the transformation and the discretization scheme. While central differences are adequate for the diffusion part, a higher-order discretization scheme which employs a three-point upstream-weighted interpolation technique (QUICK^{11,12}) is used for the convection terms; the latter splits into a first-order upwind part, being treated implicitly, and the remaining terms which are lumped into the source terms. For stability reasons, equation (10) is underrelaxed by ω ($0 < \omega < 1$) and reads

$$-\frac{A_P}{\omega} u_i^{P*} + \sum_{K=E,W,F,B} A_K u_i^{K*} + \left(S_M^i + \frac{1-\omega}{\omega} A_P u_i^{P(n)} \right) = 0, \quad i = 1, 2, \quad (11)$$

where A_P is the central node coefficient, S_M^i are the source terms and the superscripts over u_i denote the nodes where these are referred to. An asterisk denotes an intermediate velocity field which does not necessarily satisfy the continuity equation, while (n) denotes the previous iteration level. Finally, since the finite volume coefficients are common to all momentum equations, their discretized forms share a common coefficient matrix $[A]$ and read

$$[A]\{u_i^*\} = \{b_i\}, \quad i = 1, 2. \quad (12)$$

Turbulence equations

Since a coefficient matrix inversion will be inevitably charged to the momentum equations, additional inversions can be avoided by smoothing the edges among the turbulence and momentum equations so as to share the same implicit parts. A comparison of (8) and (9) shows that only different diffusion coefficients in the k and ε equations appear which involve the ratio of the eddy viscosity to the effective Prandtl number instead of the effective viscosity itself. A modification is carried out by adding the diffusion terms

$$S^\Phi = S^\Phi + \sum_{\lambda=1}^2 \frac{\partial}{\partial \xi^\lambda} \left[\left(\frac{1-\sigma_\Phi}{\sigma_\Phi} \mu_t - \mu \right) J g^{\lambda\lambda} \frac{\partial \Phi}{\partial \xi^\lambda} \right], \quad \Phi = k, \varepsilon,$$

in the source terms of the k and ε equations while retaining the five-node stencil previously used. From an algorithmic point of view the solution of the turbulence equations has to precede the solution of the continuity equation so as to take advantage of the already assembled coefficient matrix.

Pressure correction equation

In order to enforce the continuity constraint, the pressure correction method previously established for incompressible flow calculations⁷ is extended to compressible flows. The method relies on the continuity equation integrated over the same control volumes as the momentum equations, namely

$$[Jh\rho V^1]_w^e + [Jh\rho V^2]_b^f = 0. \quad (13)$$

The development of the pressure correction equation is shown in Reference 7 and only features concerning its extension to compressible flows will be elaborated here. The discretized momentum equations, providing a link between velocity and pressure, get shifted from the cell centre P to the midpoints m ($m = e, w, f, b$) of the cell faces separating P and the adjacent nodes M ($M = E, W, F, B$). Algebraic manipulations with the local metrics provide the contravariant mass

flux components (to be regarded as the convecting mass flux components normal to the cell faces), which read

$$(\rho V^\pi)_m^* = \frac{\omega}{A'_m} \left[\overline{\left(\sum_{K=E,W,F,B} A_K u_i^{K*} + \tilde{S}_M^i \right) \frac{\partial \zeta^\pi}{\partial x_i}} \right] - \frac{\omega}{A'_m} \left[\frac{\partial}{\partial \zeta^k} \left(Jh \frac{\partial \zeta^k}{\partial x_i} p \right) \right] \frac{\partial \zeta^\pi}{\partial x_i} \Big|_m + (1 - \omega) \overline{(\rho V^\pi)_m^{(n)}}, \quad \pi = 1, 2. \quad (14)$$

An overbar denotes linear averaging between P and M, while A' are the central coefficients involved in the discretized momentum equations divided by the density:

$$A'_p = \frac{A_p}{\rho_p}. \quad (15)$$

With respect to equation (11) the source term \tilde{S}_M^i is split into two parts, the first containing the pressure gradient and the second, \tilde{S}_M^i , including any other source terms. According to (14), the mass flux at a cell face consists of a linearly interpolated part and a local pressure gradient term which is centrally differenced over the cell faces to circumvent any pressure-velocity decoupling.

In order not to damage the already satisfied momentum equations, the contravariant mass flux corrections are linked to pressure correction differences through

$$(\rho V^\pi)'_m = -\frac{\omega}{A'_m} \left[\frac{\partial}{\partial \zeta^k} \left(Jh \frac{\partial \zeta^k}{\partial x_i} p' \right) \right] \frac{\partial \zeta^\pi}{\partial x_i} \Big|_m, \quad \pi = 1, 2. \quad (16)$$

By substituting (16) and (14) into (13), the pressure correction equation results, which, if only the orthogonal terms are treated implicitly, reads

$$-B_p p'_p + \sum_{K=E,W,F,B} B_K p'_K + S^* = 0, \quad (17)$$

where S^* stands for the divergence of the provisional mass flux $\varrho^{(n)} u_i^*$ field. By solving (17), the pressure is readily updated. On the other hand, both the Cartesian velocities at the cell centres (the solution field) and the contravariant mass flux components at the cell faces (the convecting field) are corrected through (16). For the former, equation (16) needs to be shifted back to the cell centres, where it must be decomposed to its constituents, namely the Cartesian velocity and the density. This is the only phase in the algorithm where the upwind-biased density is used. Following a similar approach used by Lien and Leschziner,⁶ the velocity components at the cell centres are corrected through

$$(u_i^p)' = -\left(\frac{\rho}{\tilde{\rho}} \right)_p J \frac{\omega}{A_p} \left(\frac{\partial p'}{\partial \zeta^j} \frac{\partial \zeta^j}{\partial x_\lambda} \frac{\partial \zeta^k}{\partial x_\lambda} \frac{\partial x_i}{\partial \zeta^k} \right)_p, \quad i = 1, 2, \quad (18)$$

where $\tilde{\rho}$ is the retarded density. In contrast with Reference 6, the retarded density is operating only on the velocity component correction during the pressure correction phase.

Retarded density

For transonic flow problems the retarded density $\tilde{\rho}$ is used to recover the velocity corrections from the mass flux ones at the cell centres. By reconsidering techniques springing from earlier works on transonic full potential equations, the upwind effect on the density must conform to the local flow

direction. For flows not aligned with the co-ordinate system, the upwind biasing is controlled by the directional Mach numbers

$$M^i = \frac{JV^i}{a\sqrt{g^{ii}}}, \quad i = 1, 2,$$

(no summation over i) where a is the local speed of sound.

Thus the retarded density over any cell centre P is calculated by

$$\tilde{\rho}_P = \rho_P + \kappa \sum_{i=1}^2 \left(1 - \frac{1}{(M^i)^2}\right) (\rho_{\text{up},P}^i - \rho_P), \quad (19)$$

where $\rho_{\text{up},P}^i$, $i = 1, 2$, is the upstream node of P in the i -direction, the criterion being the sign of M^i . Amplification or attenuation of the upwind biasing in density is controlled through the parameter κ ($\kappa \leq 1$).

It has to be said that the density update, which always precedes the calculation of the retarded density, is based on updating the static temperature via (6) and the state equation (5).

NUMERICAL SOLVERS

All discretized differential equations share the same form, which, for any scalar variable Φ , can be written as

$$[A]^{(n)}\{\Phi\}^{(n+1)} = \{b_\Phi\}^{(n)}, \quad (20)$$

where $\{\Phi\}$ is the vector of the solution variable (i.e. u_i^* , k , ε or p'), $[A]$ is the coefficient matrix and $\{b\}$ summarizes the source terms. Superscript (n) denotes quantities calculated at the current iteration level.

Convection–diffusion equations

In the segregated algorithm, different solvers can be used for each group of equations. As far as the transport-type equations are concerned, the solution of (20) is obtained using the modified strongly implicit procedure (MSIP),¹³ according to which the coefficient matrix $[A]^{(n)}$ is incompletely factored into an upper $[U]$ and a lower $[L]$ triangular matrix. This inversion is not costly for two-dimensional applications and is obtained recursively by requiring that $[L]$ and $[U]$ share the same structure as the lower and the upper part of $[A]$ respectively. For periodic flows such as those encountered in two-dimensional cascades, a particular modification in the scheme, analysed in the Appendix, is introduced. To obtain the dependent variables, four two-step procedures follow, which read

$$\begin{aligned} \text{step 1 : } & [L]\{\gamma_\Phi\} = \{b_\Phi\}, \\ \text{step 2 : } & [U]\{\Phi\} = \{\gamma_\Phi\}, \quad \Phi = u_i^*, k, \varepsilon, \quad i = 1, 2. \end{aligned} \quad (21)$$

Pressure correction equation

The pressure correction equation is solved using incomplete LU factorization combined with an overall parameter accelerating the convergence. This parameter β is calculated once per iteration through⁷

$$\beta = \frac{\alpha_1}{\alpha_1^2 + \alpha_2^2},$$

where

$$\alpha_1 = \left([P]^{-1}[B] \frac{[P]^{-1}\{S^*\}}{\|[P]^{-1}\{S^*\}\|} \right) \cdot \frac{[P]^{-1}\{S^*\}}{\|[P]^{-1}\{S^*\}\|}, \quad \alpha_2 = \left\| [P]^{-1}[B] \frac{[P]^{-1}\{S^*\}}{\|[P]^{-1}\{S^*\}\|} - \alpha_1 \frac{[P]^{-1}\{S^*\}}{\|[P]^{-1}\{S^*\}\|} \right\|,$$

and p' is updated through

$$\{p'\} = \beta[P]^{-1}\{S^*\}, \quad (22)$$

where $[P]$ is an approximate inverse of $[B]$ calculated through the LU factorization.

RESULTS AND DISCUSSION

Two-dimensional, controlled diffusion aerofoil compressor cascade

As a first case, the flow in a two-dimensional, controlled diffusion aerofoil cascade, which is representative of the first rotor hub section of industrial axial compressors, will be analysed with the present method. The analysis will be carried out under four flow conditions, the design conditions being one of them. A detailed discussion on this cascade can be found in Reference 14, where the exact aerofoil geometry is also included. The pitch-to-chord ratio is equal to 0.68 and the stagger angle is equal to 30° .

The aerofoil's design conditions correspond to an inlet flow angle of 47° at an inlet Mach number equal to 0.62. In the aforementioned paper the axial velocity–density ratio (AVDR) was given equal to approximately 1.1. To account for the AVDR effect on the flow, a streamtube thickness variation of -10 per cent, linearly distributed between the axial co-ordinates corresponding to the leading and trailing edges, was introduced in the calculations, since no other information was available. The streamtube thickness was held constant upstream of the leading edge and downstream of the trailing edge at its corresponding values at the leading and trailing edges respectively. The grid used in the calculations consists of 170×51 nodes in the streamwise and pitchwise directions, respectively and is illustrated in Figure 2.

The four flow conditions to be analysed herein correspond to an incidence variation from -7° up to 5° . While the inlet flow angle was introduced directly in the calculations, the exit pressure was calculated by means of the known exit-to-inlet static pressure ratio, the inlet Mach number and the inlet stagnation pressure, which was held constant at 125,000 Pa at a stagnation temperature of 288 K. The molecular viscosity was kept constant throughout the flow field.

In Table 1 the flow data quantities are summarized on a case-by-case basis. In the same table the predicted and measured values of the exit-to-inlet static pressure ratio, inlet Mach number, exit flow angle and cascade losses are tabulated. The latter is defined as

$$\omega = \frac{P_{t1} - P_{t2}}{P_{t1} - P_1},$$

where subscripts 1 and 2 denote the inlet and exit respectively.

The same compressor cascade has been analysed previously by an explicit time-marching, primitive variable Navier–Stokes code.¹⁵ In that study, by alternatively using the low-Reynolds-number $k-\varepsilon$ and Baldwin–Lomax models, it was concluded that the $k-\varepsilon$ model provides more accurate loss predictions but underestimates the flow turning by approximately 1° . On the other hand, the Baldwin–Lomax model underestimated the level of losses but provided excellent predictions of the exit flow angles, even though the results were noticeably affected by the transition criterion incorporated.

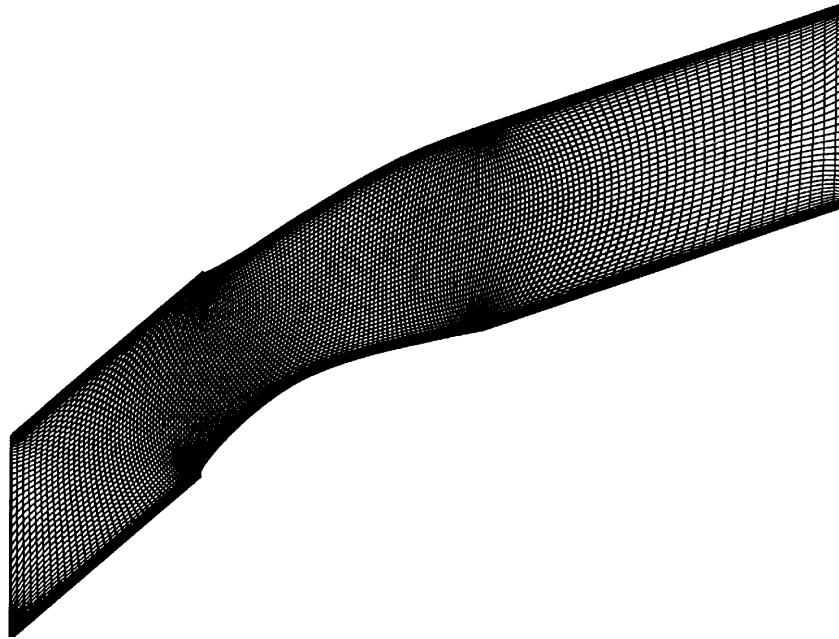


Figure 2. Compressor cascade grid

The results predicted by the present method are in very good agreement with measurements, with the exception of the high-positive-incidence case ($\alpha_1 = 52^\circ$) where the turbulence model in use is proved inadequate. For the design conditions ($\alpha_1 = 47^\circ$) and the low-negative-incidence case ($\alpha_1 = 43^\circ$) the predicted losses are in excellent agreement with measurements, while the discrepancy between predicted and measured exit flow angles is less than 0.5° . In the higher-negative-incidence case ($\alpha_1 = 40^\circ$) the agreement in the exit flow is perfect and the losses are twice as high as those corresponding to the design conditions; the present method overpredicts the loss level by approximately 15 per cent. In the same case the peak velocity over the suction side is located at approximately 45 per cent of the chord. This is also in perfect agreement with measurements, as

Table I

α_1 ($^\circ$)	40	43	47	52
i ($^\circ$)	-7	-4	0	5
Re (10^5)	8.61	8.59	8.41	7.63
AVDR	1.0845	1.0909	1.1021	1.1032
M_1 (experiment)	0.6229	0.6184	0.6180	0.6214
M_1 (prediction)	0.6124	0.6102	0.6125	0.6383
P_2/P_1 (experiment)	1.0619	1.0948	1.2121	1.1459
P_2/P_1 (prediction)	1.0530	1.0876	1.1172	1.1618
ω (experiment)	0.0466	0.0232	0.0186	0.0417
ω (prediction)	0.0542	0.0226	0.0185	0.0226
α_2 (experiment)	21.52	20.18	20.20	22.81
α_2 (prediction)	21.48	20.56	20.63	22.64

depicted in Figure 3, where the isentropic Mach number distributions along the pressure and suction sides of the blade are illustrated for all cases examined. The maximum velocity location is followed by a severe flow deceleration; no important back-flow was captured by the present calculation.

In the high-positive-incidence case, even if the exit flow angle is satisfactorily predicted, the loss level remains quite low compared with the measured one, though increased compared with the nominal conditions. The modelling of the velocity profiles in the near-wall region through the wall function technique seems to be the main reason for the above discrepancy. An improvement in the flow prediction in this case, without altering the near-wall treatment, was accomplished through the modification of the turbulence model constants. Two variants have been tested, both based on increasing the production term in the ε equation. In practice this was carried out by shifting the coefficient c_1 to a higher value (1.57 rather than 1.43) in two ways: (a) only in the separated region as in Reference 16, using a simplistic criterion for the definition of the recirculation zone, and (b) in the entire flow field. Results in better agreement with experiment have been obtained in case (b), where the isentropic Mach number distribution along the suction side was affected even upstream of the onset of separation, and are those presented herein. Apart from discrepancies occurring in the separated regions, mainly attributed to the inadequacies of the turbulence model, the fact that the loss level is accurately captured by a full Navier–Stokes code implies that the transition must have occurred too close to the leading edge.

In Figure 4 the convergence history for the $i = 0^\circ$ case is presented for all equations resolved. One may observe a very fast, linear, up to machine accuracy, tendency, with the exception of the very first iterations (approximately 500 iterations) where the arbitrary initial field effects are overcome. From an engineering point of view, approximately 2000 iterations are sufficient for a well-converged solution. The CPU time per node and iteration is about 0.07 ms on a single MIPS 8010 processor. The convergence history illustrated in Figure 4 was obtained by using underrelaxation factors equal to 0.6 for the momentum, pressure correction and turbulence equations. In the high-positive-incidence case the convergence is quite similar; the underestimation of the separated zone alleviates any difficulty associated with flow unsteadiness, often caused by massively separated flows.

Two-dimensional, steam turbine cascade

The second case examined is that of an SE1050 cascade designed for the last stage of a SKODA steam turbine,¹⁷ featuring a stagger angle of 37.11° , a chord of 0.1 m and a pitch-to-chord ratio of 0.55117. This case is analysed using air as the working fluid, under two flow conditions corresponding to exit isentropic Mach numbers M_{2is} of 0.906 and 1.189 respectively. In both cases the inlet flow angle is 19.3° , which corresponds to zero incidence, and the inlet stagnation conditions were set to 99,000 Pa and 288 K. The H-type grid used in the calculations consists of 126×41 nodes and is illustrated in Figure 5.

In Figure 6 the critical Mach number distributions along the pressure and suction sides of the blade are plotted, which are in good agreement with the measured distributions for both cases. The suction-side distribution reaches sonic conditions at approximately 45 per cent of the chord. In this part of the blade the flow accelerates smoothly from the theoretical leading edge and reaches sonic conditions in exactly the same way in both cases. In the $M_{2is} = 1.189$ case the supersonic expansion that follows appears as a decrease and a further increase in the flow velocity, in the part of the flow between 45 per cent and 80 per cent of the blade chord, over the suction side, mostly related to the curvature of the suction side at about 50 per cent of the chord. In this case the acceleration is terminated by the shock wave originating from the neighbouring profile. The interaction with the incident shock slows down the expansion, which tends to show up again close to the trailing edge. Since the last part of the blade's suction side, following the location of the maximum curvature, is also straight, the trailing

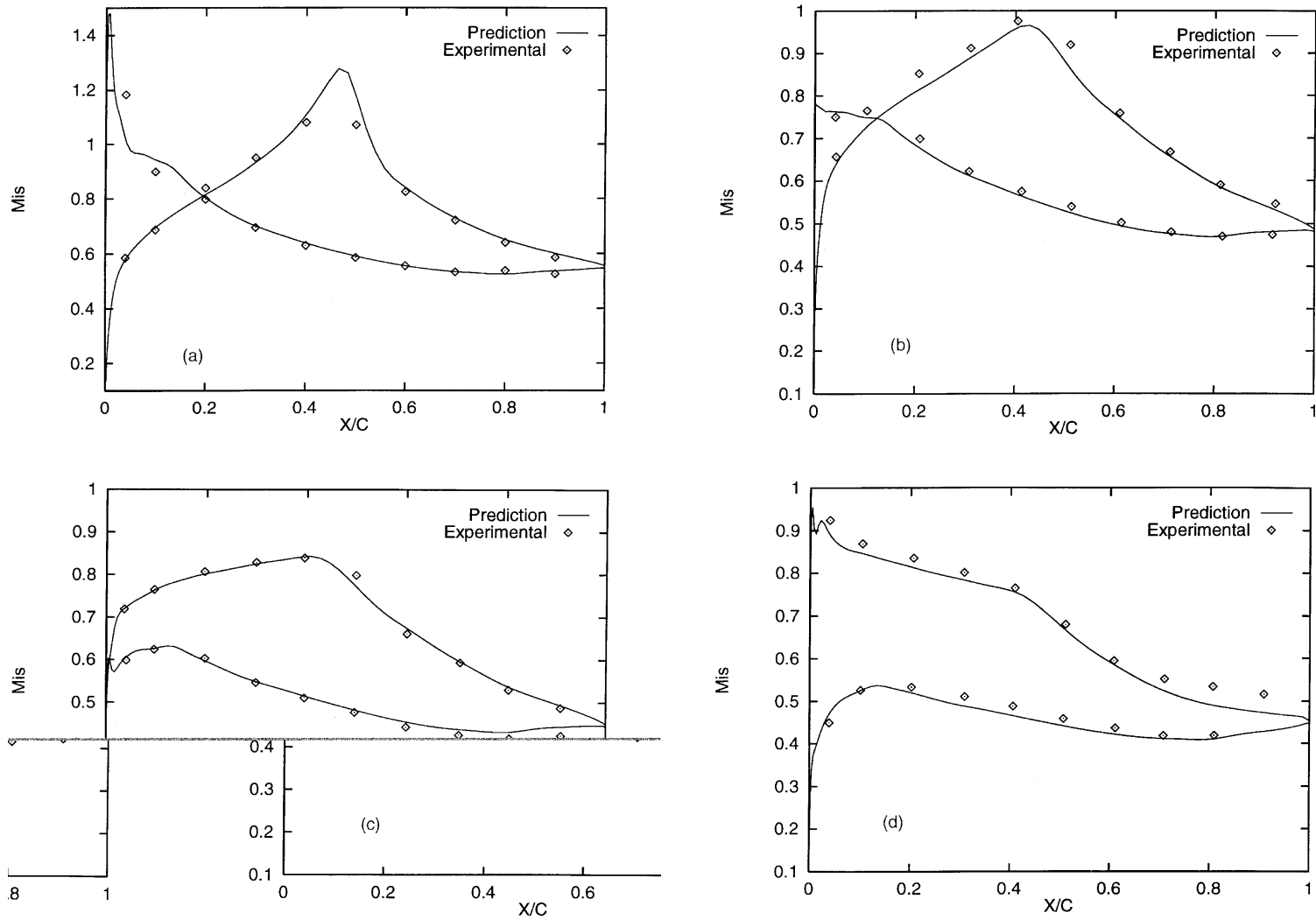


Figure 3. Isentropic Mach number distribution along blade: (a) $i = -7^\circ$; (b) $i = -4^\circ$; (c) $i = 0^\circ$; (d) $i = 5^\circ$

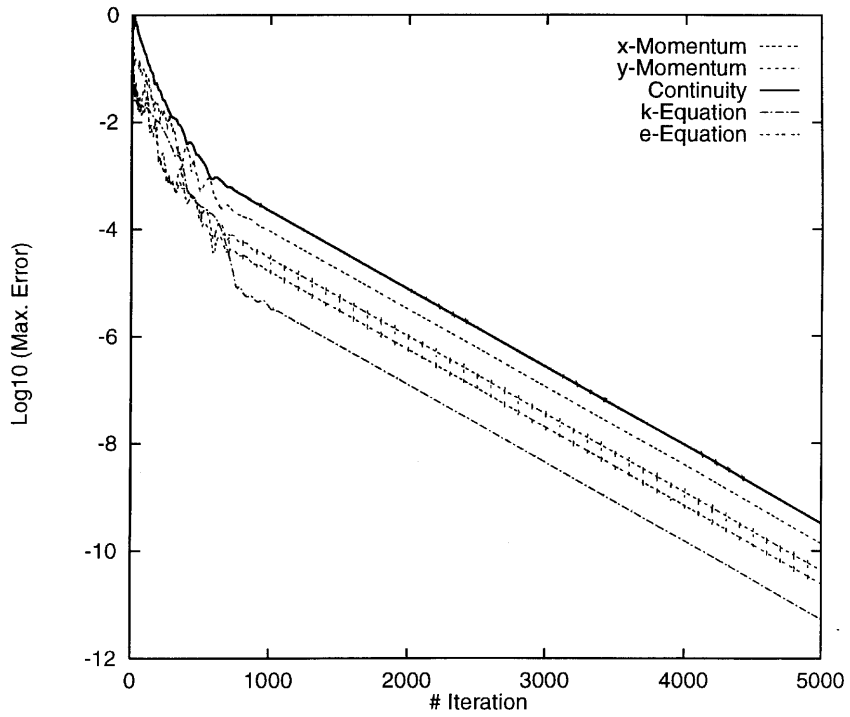


Figure 4. Convergence history for all equations in $i=0^\circ$ compressor cascade case

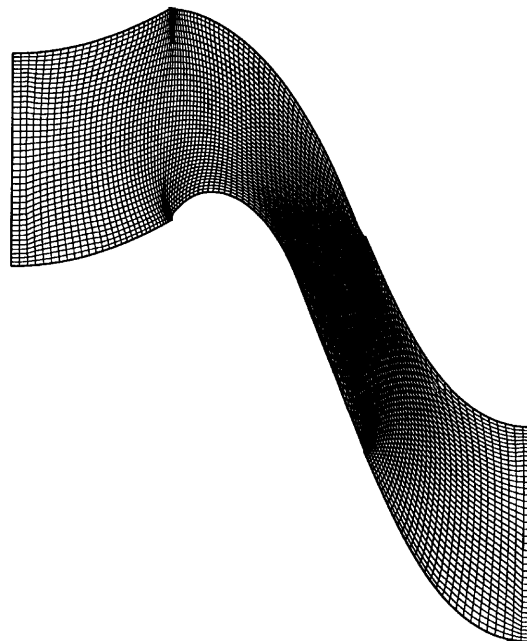


Figure 5. Turbine cascade grid

edge effects are local, without dominating over the entire flow field. On the other hand, the flow acceleration over the pressure side is monotonic as well as identical in the major part in both cases examined. The two measured and two predicted distributions remain identical in the first 90 per cent of the blade chord. Only in the last 10 per cent, close to the rounded trailing edge, is the flow in the $M_{2is} = 1.189$ case much more accelerated than in the milder case. The predicted very steep acceleration is in full agreement with the measured one. In Figure 7 the calculated iso-Mach contours are presented in both cases, aimed at shedding some more light on the aforementioned issues. Compared with the available interferometric pictures of the flows (these are provided in Reference 17 and will not be repeated here), these figures show that the calculations reproduce reasonably well the major characteristics of the flows. To illustrate the algorithm's merits, the convergence history for all equations is plotted in Figure 8 for the $M_{2is} = 0.906$ case; the maximum error is plotted appropriately normalized on the initial error. One can easily observe the very fast, monotonic trend with a slight waviness which is a common feature of segregated solution methods. Similar characteristics can be depicted in the $M_{2is} = 1.189$ case.

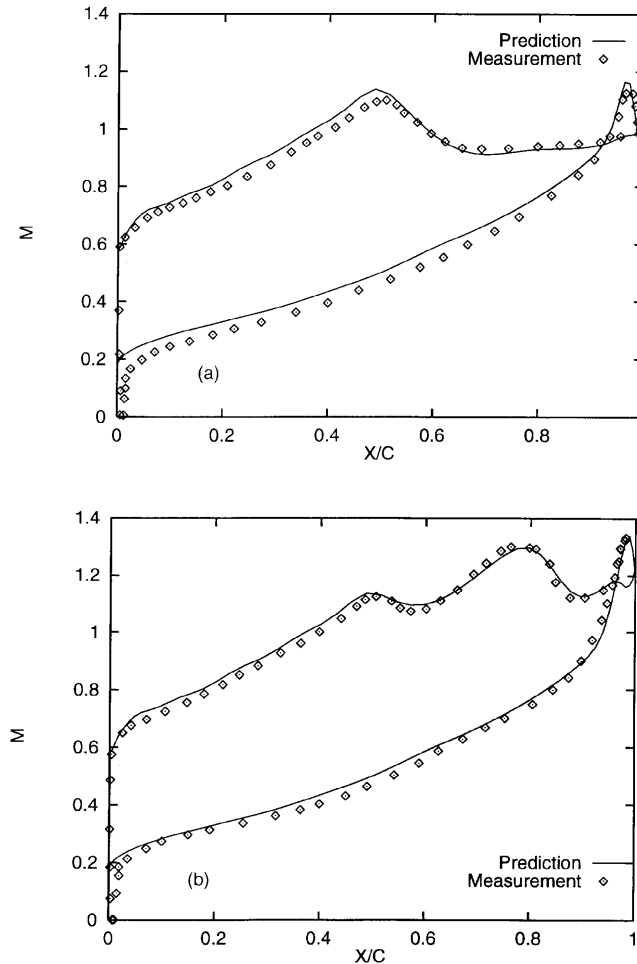


Figure 6. Critical Mach number distribution along blade for turbine case: (a) $M_{2is} = 0.906$; (b) $M_{2is} = 1.189$

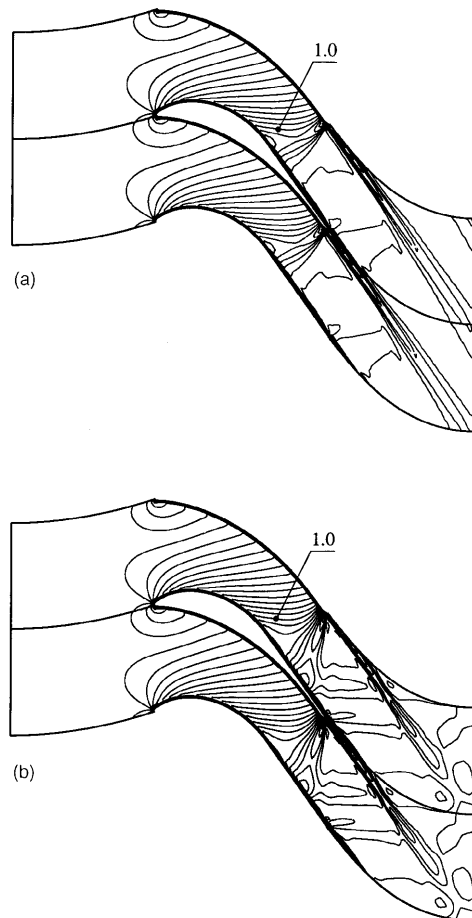


Figure 7. Iso-Mach contours at turbine cascade passage (increment 0.05): (a) $M_{2is} = 0.906$; (b) $M_{2is} = 1.189$

CONCLUSIONS

A pressure correction method for the solution of two-dimensional turbulent flow fields, previously utilized for the prediction of laminar and turbulent incompressible flows, has been extended to the transonic regime. The momentum equations are still solved in the Cartesian velocity components, so that the main algorithmic part of the method (discretization and numerical solvers) remains the same. The pressure correction equation enforces the satisfaction of the continuity equation by correcting the convecting mass flux field at the cell faces and the Cartesian velocities at the cell centres. There, the retarded density is used to adapt the type of governing equations to the physics of the flow.

The method exhibits fast convergence properties by forming the same coefficient matrix for all but the pressure correction equations. The segregated solution of the governing equations, coupled with appropriate fully implicit solvers, is proved very efficient. An appropriate choice of the underrelaxation factors in all equations results in a monotonic convergence.

The method has proved capable of predicting complex turbomachinery flows in compressors and turbine cascades under design and off-design conditions. Further improvement in the presented

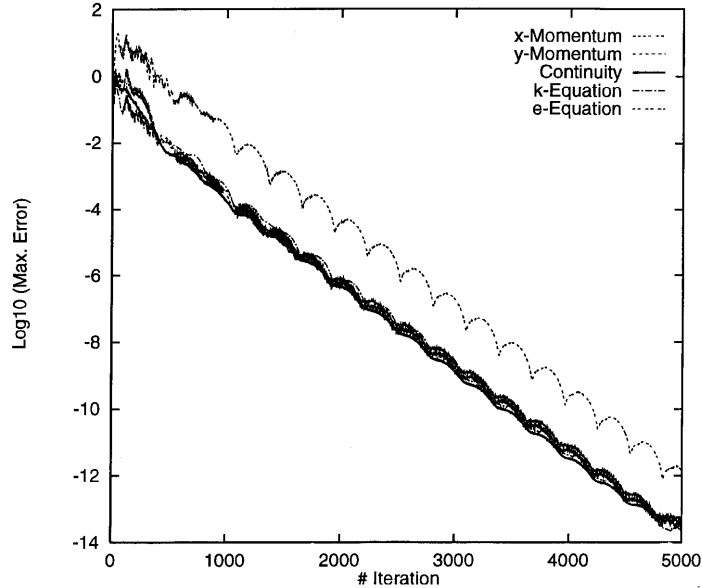


Figure 8. Convergence history for all equations in $M_{2is} = 0.906$ turbine case

results under off-design conditions with extensive back-flow regions can be obtained by improving the turbulence model, which is beyond the scope of the present paper.

APPENDIX A: PERIODIC INCOMPLETE LU SCHEME

For problems not involving periodicity or for periodic problems where periodicity is explicitly handled, a five-node discretization scheme leads to the standard five-diagonal coefficient matrix $[A]$. For H-type grids, modifications to the matrix structure should be introduced and a seven-diagonal matrix should be formed if periodicity is to be treated implicitly.

In a cell-centred approach, if $I \times J$ is the grid dimension, $(I - 1) \times (J - 1)$ variables are to be stored and this is performed using the following numbering convention:

$$k = (i - 1)(J - 1) + j, \quad 1 \leq i < I, \quad 1 \leq j < J. \quad (23)$$

Under the periodicity-induced modifications the seven-diagonal form of $[A]$, corresponding to the notation of Figure 9, is given schematically in Figure 10, where the broken lines denote extra entries not appearing when the five-node discretization scheme is applied. In the same figure the incomplete factorization of $[A]$ into an upper and lower triangular matrix¹³ is shown.

According to the numbering system (23), the periodicity along the lower and upper rows of nodes (see Figure 11) requires that the corresponding matrix entries D (for the lower part, P1) and F (for the

C	F	
B	E	H
	D	G

Figure 9. Stencil notation used in incomplete LU decomposition

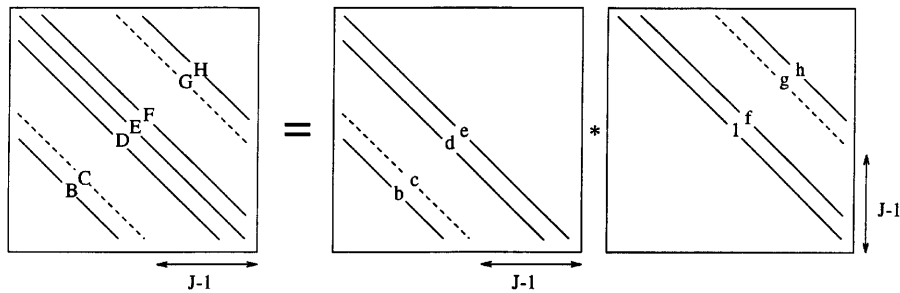


Figure 10. Schematic factorization of coefficient matrix into lower and upper matrices

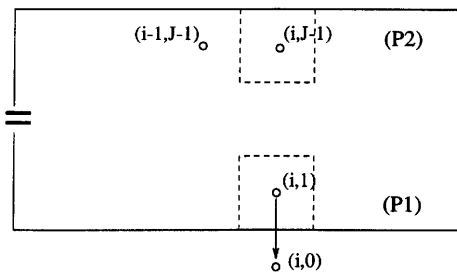


Figure 11. Periodic nodes in transformed plane

upper part, P2) are handled through the diagonals G and C respectively. These are the only non-zero entries emerging in these diagonals. Following the Schneider and Zedan¹³ scheme, the resulting triangular matrices $[L]$ and $[U]$ have the same structure as the lower and upper triangular parts of $[A]$. Although C and G are very sparse diagonals, the resulting diagonals c and g are dense owing to the recursive algorithm implemented in their calculation. Attention must also be paid to the application of the 'modified' SIP, where Taylor expansions between adjacent nodes are implemented. The gain using the periodic MSIP scheme is estimated at approximately 10 per cent of the computational time.

REFERENCES

1. R. I. Issa and F. C. Lockwood, 'On the prediction of two-dimensional supersonic viscous interactions near walls', *AIAA J.*, **15**, 182–188 (1977).
2. K. C. Karki and S. V. Patankar, 'Pressure based calculation procedure for viscous flows at all speeds in arbitrary configurations', *AIAA J.*, **27**, 1167–1174 (1989).
3. J. J. McGuirk and G. J. Page, 'Shock capturing using a pressure-correction method', *AIAA J.*, **28**, 1751–1757 (1990).
4. G. Zhou and L. Davidson, 'Transonic flow computations using a modified SIMPLE code based on collocated grid arrangement', in *Computational Fluid Dynamics 1992*, Vol. 2, 1992, pp. 749–756.
5. I. Demirdzic, Z. Lilek and M. Peric, 'A collocated finite volume method for predicting flows at all speeds', *Int. j. numer. methods fluids*, **16**, 1029–1050 (1993).
6. F. S. Lien and M. A. Leschziner, 'A pressure-velocity solution strategy for compressible flow and its application to shock/boundary-layer interaction using second-moment turbulence closure', *J. Fluids Eng.*, **115**, 717–725 (1993).
7. K. C. Giannakoglou and E. S. Politis, 'A segregated implicit solution algorithm for 2-D and 3-D laminar incompressible flows', *Int. j. numer. methods fluids*, **21**, 1067–1086 (1995).
8. C. Hirsch, *Numerical Computation of Internal and External Flows*, Wiley, Chichester, 1990.
9. W. P. Jones and B. E. Launder, 'The prediction of laminarization with a two-equation model of turbulence', *Int. J. Heat Mass Transfer*, **15**, (1972).

10. S. Majumdar, 'Role of underrelaxation in momentum interpolation for calculation of flow with nonstaggered grids', *Numer. Heat Transfer*, **13**, 125–132 (1988).
11. B. P. Leonard, 'A stable and accurate convective modelling procedure based on quadratic upstream interpolation', *Comput. Methods Appl. Mech. Eng.*, **19**, (1979).
12. T. Hayase, J. A. C. Humphrey and R. Greif, 'A consistently formulated QUICK scheme for fast and stable convergence using finite-volume iteration calculation procedures', *J. Comput. Phys.*, **98**, (1992).
13. G. E. Schneider and M. Zedan, 'A modified strongly implicit procedure for the numerical solution of field problems', *Numer. Heat Transfer*, **4**, 1–19 (1981).
14. W. Steinert, B. Eisenberg and H. Starke, 'Design and testing of a controlled diffusion airfoil cascade for industrial axial flow compressor applications', *ASME Paper 90-GT-140*, 1990.
15. C. Vassilopoulos, G. Simandirakis, K. C. Giannakoglou and K. D. Papailiou, 'Losses prediction in axial flow compressor cascades using an explicit $k-\epsilon$ Navier–Stokes solver', *Proc. 85th PEP/AGARD Symp. on Losses Mechanisms and Unsteady Flows in Turbomachines*, Derby, May 1995.
16. G. Simandirakis, C. Vassilopoulos, K. C. Giannakoglou and K. D. Papailiou, '2-D transonic bump flow calculations using an explicit fractional-step method', *Proc. Efficient Turbulence Models for Aeronautics (ETMA) Workshop*, Manchester, November 1994, Vieweg, Braunschweig, 1997.
17. M. Stastny and P. Safarik, 'Experimental analysis data on the transonic flow past a plane turbine cascade', *ASME Paper 90-GT-313*, 1990.